NTNU
Norwegian University of
Science and Technology

Variable Flux Permanent Magnet Synchronous Machines: Building and Testing Simple Designs with High-Coercivity Magnets

Kasper Kvinnesland

Master of Energy and Environmental Engineering
Submission date: July 2018
Supervisor: Robert Nilssen, IEL

Norwegian University of Science and Technology
Department of Electric Power Engineering

Variable Flux Permanent Magnet Synchronous Machines: Building and Testing Simple Designs with High-Coercivity Magnets

Kasper Kvinnesland

Supervisor: Robert Nilssen, NTNU

***Abstract*—Variable flux permanent magnet synchronous machines (VF-PMSMs) use a novel operation concept based on changing the magnetization level of the permanent magnets in accordance with variations in speed and torque. This may improve the efficiency of wide-speed operation, reducing or removing the need for flux weakening current to counter-act excessive back-emf at high speeds. Magnetization change in these machines is achieved through short d-axis current pulses into the stator windings. The technology has gain increased attention the last few years, having numerous publications attempting to solve the various challenges related to design and operation. This paper will first give a conceptual introduction to VF-PMSMs and briefly summarize some of the literature published on various designs. Then, partly based on the findings of others, two simple VF-PMSM rotors are designed and built to fit a pre-existing stator. A rotor built with only strong samarium-cobalt magnets had its viability as a VF-PMSM experimentally tested. Results show that the magnet material used is stronger than ideal and that laminating the rotor may be crucial for functional VF-PMSM designs.**

I. Introduction

Permanent magnet synchronous machines (PMSMs) offer high efficiency and high torque density, which have made them increasingly popular over the last few decades. In certain applications, however, a significant disadvantage of PMMs is limited operation above rated speed. Since the rotor magnetomotive force (mmf) is constant, high speed operation may induce too large back-emf in the stator windings and cause overvoltage, potentially damaging the windings or inverter. In the main competitor of PMSMs, the induction machine, the rotor mmf can be controlled freely, such that excessive back-emf will not become a problem.

A common method to achieve high-speed operation of PMSMs is to inject continuous negative d-axis current, i.e. field weakening current, to lower the emf induced by the rotating rotor flux. This extra stator current increases copper losses and, therefore, the efficiency decreases when conventional PMSMs is operated above rated speed. Furthermore, since the current capability of the inverter and stator windings is limited, there will be an upper limit to the speed for which field weakening can be used to avoid excessive back-emf.

Various designs have been explored and used to overcome the problem of constant rotor flux. Such machines are called flux-adjustable permanent magnet machines (FAPMMs), and a thorough review of the various FAPMMs has recently been presented in [1]. Perhaps the most common FAPMM design is the utilization of hybrid excitation, usually achieved by adding field windings on the rotor in series or parallel with the permanent magnets (PMs). The field coil current can then be controlled to increase or decrease the resulting air gap flux in accordance with operating conditions, allowing for a wider operating range. However, this requires more circuitry and the additional field current increases copper losses.

An alternative to such hybrid designs is to manipulate the magnetization state of the PMs, by injecting large current pulses in the stator windings. The ability to control the level of magnetization in the rotor magnets allows manipulation of air gap flux to optimally correspond with the operating point, without more circuitry or continuously feeding loss-inducing current. Machines manipulating the magnetization of the rotor PMs are called variable flux permanent magnet synchronous machines (VF-PMSMs) and was first introduced in [2]. Machines of this kind are also referred to as memory motors, variable magnetomotive force machines, or variable flux machines. Since the first memory motor was proposed, a substantial amount of research has been focused on this design and its extensions.

First, this paper aims to describe the general operation of VF-PMSMs. Here, the scope is limited to machines using the stator windings as the sole source of magnetization current, having an inner rotor, radial structure. Various memory machines using dedicated magnetization coils, mounted on either rotor or stator is dealt with in [1], and will not be considered here. The purpose is to provide an explanation of the operational concept of VF-PMSMs and give a short overview of the state-of-the-art research within the field, so as to serve as a straightforward introduction to this relatively new technology.

The ferromagnetic theory necessary to understand the behavior of VF-PMSMs will be presented first. Then, magnet materials suitable for VF-PMSMs will be discussed, followed by an explanation of the operational principle of basic PMSMs and VF-PMSMs. Various designs that have been researched elsewhere will be shortly reviewed, before a novel design topology, with emphasis on making the manufacturing cheap

and uncomplicated will be developed.

In existing literature, little has been written about the building process of VF-PMSMs. Furthermore, there is a lack of detailed discussion on PM material properties suitable for this use. Therefore, the main goal of this investigation is to thoroughly describe the full design and building process of a simple VF-PMSM, and to experimentally demonstrate the basic functionality of such a machine, emphasizing the importance of the magnet material being used. Specifically, the experimental investigation is conducted using high-coercive Samarium-Cobalt (SmCo) magnets.

Sections II-VI are largely taken from a review of VF-PMSMs written earlier by the author. [3]

II. Ferromagnetic Magnetization Theory

Understanding the magnetization behavior of the PM-material is essential to properly design and operate VF-PMSMs. This behavior is best described by the magnetization curve, the so-called BH-curve, of the different materials. An example of such a curve is shown in Fig. 1 for a ferromagnetic material. Here, B_s is the saturation flux density; the highest possible flux density the material can achieve with a positive external field. B_r is the remanent flux density; the remaining flux density when the material is first brought to saturation by an external field before reducing the field to zero. H_c is the coercive force; the external field necessary to make the flux density through the material zero, after it has been fully magnetized.

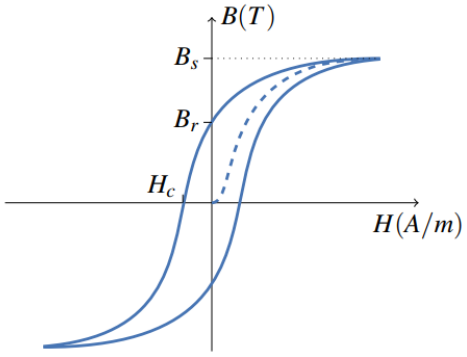

Fig. 1: Magnetization curve of an arbitrary ferromagnetic material [4].

The cause of this behavior in ferromagnetic materials is found on the microscopic scale. These materials consist of magnetic domains that individually produce a magnetic field in some arbitrary direction. Under normal circumstances, the domains in a piece of ferromagnetic material are randomly aligned and produce no macroscopic magnetic effect. However, if an external field gives rise to magnetic flux through the material, the domains can align to produce a net magnetic field in the direction of the external field. After the external field is removed, some portion of the domains will remain in the given direction, producing a net positive flux. This is why the curve in Fig. 1 crosses the B-axis at B=B_r instead of the origin. This phenomenon is described mathematically by Eqs. 1 and 2, where $\mathbf{B}$ is the magnetic flux density vector, $\mathbf{H}$ is the magnetic field vector, $\mathbf{M}$ is the magnetization vector, μ_0 is the permeability of vacuum and μ_r is the relative permeability of the material.

$$\mathbf{M} = (\mu_r - 1)\mathbf{H} \tag{1}$$

$$\mathbf{B} = \mu_0(\mathbf{H} + \mathbf{M}) \tag{2}$$

In ferromagnetic materials, the relative permeability is a function of magnetization. For low magnetization levels, many domains are ready to align with an external field, making $\mu_r >> 1$. This means that flux increases steeply with applied field. However, since the number of domains are limited, the magnetization has a saturation value. As the magnetization approaches this saturation value, μ_r approaches 1 and the flux density almost stops increasing with increasing field, as seen in Fig. 1.

Permanent magnet materials used in electric machines are normally "hard" ferromagnetic materials, meaning that they have high remanent flux B_r and coercive force H_c. This means that they can supply high rotor flux density while withstanding strong external fields. Permanent magnets are normally operated in the second quadrant of the BH-curve. It is important to note that even if the flux in the permanent magnet is brought down to zero by an external field, demagnetization has not necessarily occurred in the magnet. An applied field $H = H_c$ only implies that the sum of the fluxes from the magnetic field and the magnetization, is zero. Or, in terms of Eq. 2, $\mathbf{H}$ and $\mathbf{M}$ are equal in strength and opposite in direction, making $\mathbf{B}$ zero.

The external magnetic field strength necessary to demagnetize the magnet is called the *intrinsic* coercivity, or intrinsic coercive force. The intrinsic BH-curve, then, describes how the magnetization state of the PM is affected by the external field. The second and third quadrant of both the normal and the intrinsic BH-curve of a typical permanent magnet is displayed in Fig. 2. Here, H_{cJ} is the intrinsic coercive force and $I_m = \mu_0 M$ is the intensity of magnetization in the magnet. The intrinsic curve is I_m plotted against H. As can be seen from the intrinsic curve, the magnetization of the PM will not be visibly affected by an external field $H = H_c$. This means that the flux in the magnet can be reduced to zero without causing demagnetization. However, when the field approaches H_{cJ}, the magnet material is rapidly demagnetized. The point at which demagnetization initializes can be identified from the "bend" in the normal BH-curve, the so-called knee-point.

One should note that the curves in Fig. 2 are idealistic in the sense that no demagnetization seem to occur at all before the field approaches H_{cJ}. In reality, some of the magnetic domains within the material will be rotated to align with $\mathbf{H}$, even for low field strengths. Realistically, then, the intrinsic curve should have some slope for any negative value of H, and as such, the normal BH-curve should bend increasingly downwards, and not be a straight line up until the knee point. However, for strong magnets the normal BH-curve can often be approximated to be a straight line from B_r to H_c. [4]

If partial demagnetization has occurred, the PM will produce a lower flux density than before once the external field is

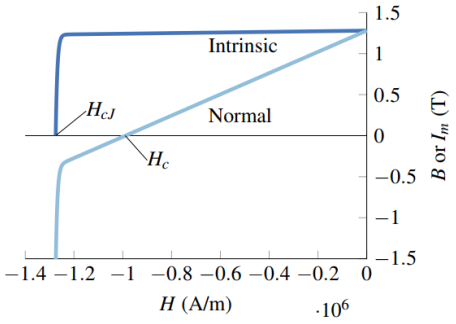

Fig. 2: Intrinsic and normal BH-curve of a typical permanent magnet. [4].

reduced to zero. That is, it will no longer produce a flux density $B = B_r$ when $H = 0$. If full demagnetization happens, by applying $H = H_{cJ}$, the PM will not supply any flux at all. Depending on the amount of demagnetization, the flux density will recoil back somewhere below B_r on the B-axis. If the PM is to have its magnetization increased again, an external field $\mathbf{H}$, now in the same direction as $\mathbf{M}$, must be applied. To illustrate this mechanism, the typical magnetization behavior of low-coercive force (LCF) magnets is shown in Fig. 3.

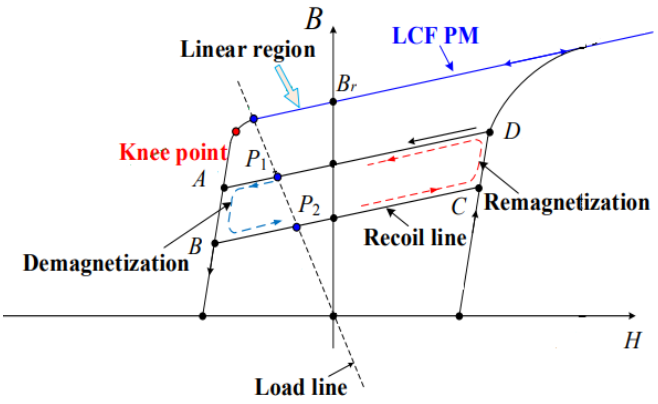

Fig. 3: General demagnetization and remagnetization behavior of low-coercive force magnets. [5]

In Fig. 3, the magnet is first operating at P_1. An external, opposing field is gradually applied, bringing the magnet to the demagnetization limit at point A. Slightly increasing the field further partially demagnetizes the magnet, bringing it to point B. Once the external field is removed, the magnet will operate at point P_2. To bring the magnet back to its former magnetization an external field in the other direction can be applied, bringing the magnet to the remagnetization limit at point C, before a further field increase causes remagnetization to point D. Once the external field is removed, the magnet will once again operate at point P_1.

PMSMs are traditionally designed to avoid demagnetization of the rotor magnets, since it will negatively impact performance, and the machine is normally not designed with the ability to remagnetize the PMs. In VF-PMSMs, on the other hand, the cycle of demagnetization and remagnetization shown in Fig. 3 is essential for optimal operation.

III. PM Material for VF-PMSMs

When designing a PMSM, there are several materials that can serve as a permanent magnet, and the choice is affected by several factors. Materials vary in price, remanent flux and coercive force. The latter two are often significantly affected by operating temperature.

What separates the VF-PMSM from other PMSMs, is its ability to manipulate the magnetization $\mathbf{M}$ of the rotor magnets while operating. The most commonly used magnets for PMSMs must be magnetized *before* they are mounted on the rotor, posing a challenge to manufacturing. Furthermore, their magnetization cannot normaly be changed (at least not in a controlled manner) once the machine is assembled. To achieve magnetization control, VF-PMSM designs tend to use other magnet materials than conventional machines. Most importantly, VF-PMSM magnets should have low intrinsic coercivity to lower the magnetization current needed to change the magnetization level. A general comparison of LCF materials is shown in Fig. 4.

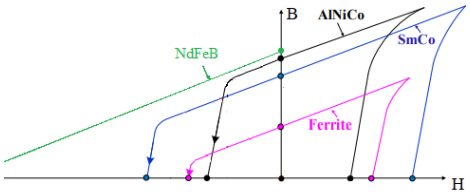

Fig. 4: Magnetization curves of common permanent magnet materials. [5]

One should note that each of the four materials in Fig. 4 have many different variations, with different BH-characteristics. However, the overall pattern seen in Fig. 4 is usually correct: NdFeB magnets have the highest remanence and is most resistant to external fields, SmCo magnets have somewhat lower remanence and coercivity; ferrite magnets have low values of both remanence and coercivity; AlNiCo magnets can have very high remanent flux, but also have extremely low intrinsic coercivity, being most easily demagnetized. It should also be mentioned that neodymium (Nd) and samarium (Sm) are rare-earth elements, making the price of these two magnet types significantly higher than others. Furthermore, NdFeB magnets are very vulnerable to corrosion and often needs a protective coating to avoid reaction with the environment. Ceramic magnets are very cheap and resistant to corrosion, making them highly popular in small machines where high rotor flux and coercive force is not top priority. Still, NdFeB and SmCo are the most commonly used PMs in high-performance applications [6], [7]. Despite its remarkable remanent flux, AlNiCo is rarely used in conventional PMSMs, but its low intrinsic coercivity makes manipulation of magnetization easy, and can therefore be useful in some VF-PMSM designs.

IV. Basic PMSM Structure and Operation

VF-PMSMs are often structurally similar to standard PMSMs and the operation principles are much the same. These basic principles should therefore be considered before discussing the specific traits unique to VF-PMSMs.

A simple three-phase PMSM machine configuration is shown in Fig. 5. Here, each phase winding is assumed to be sinusoidally distributed throughout the stator so as to simplify the analysis. These three windings can be represented by two hypothetical windings; a q-winding and a d-winding. The d-winding rotates so that its axis is always aligned with the rotor north-pole. The q-winding also rotates, keeping its axis 90 degrees ahead of the d-axis, in the direction of rotation. Using this reference frame is useful for control purposes.

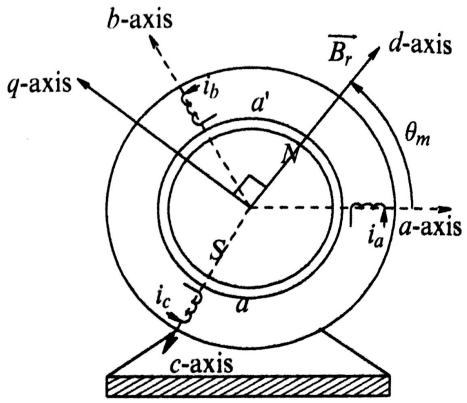

Fig. 5: A simple three-phase, two-pole PMSM. [8]

The steady state voltage in the d- and q-axis windings, neglecting the effect of stator resistance, is given by

$$v_{sd} = -\omega_m L_s i_{sq} \tag{3}$$

$$v_{sq} = \omega_m (L_s i_{sd} + \lambda_{fd}) \tag{4}$$

where ω_m is the rotor speed in electrical radians per second, L_s is the synchronous inductance, λ_{fd} the portion of the d-axis flux linkage caused by the rotor flux $\mathbf{B_r}$, and i_{sd} and i_{sq} is the current flowing in the d-winding and q-winding, respectively.

The RMS phase winding voltage is then found by

$$V_a = \frac{1}{3}\sqrt{v_{sd}^2 + v_{sq}^2} \tag{5}$$

Eqs. (3)-(5) show that an increase in rotor speed will require higher phase voltages. High-speed operation may therefore cause overvoltages on the terminals and damage windings or inverter. Flux weakening is conventionally used to avoid this problem. Most commonly this is achieved by injected a negative d-axis current to oppose the rotor flux linking the d-winding. As seen from Eq. 4, a negative d-axis current will lower v_{sq} and contribute to keeping the terminal voltage within its limits.

Torque production in a non-salient PMSM is given by

$$T_{em} = \frac{p}{2}\lambda_{fd} i_{sq} \tag{6}$$

V. VF-PMSM Operation Principle

The first VF-PMSM design was proposed in 2001 and is shown in Fig. 6 [2]. The non-magnetic barrier between each pole pair on the rotor prevents q-axis flux from going through the PMs. This ensures that the load current will not cause unintended demagnetization.

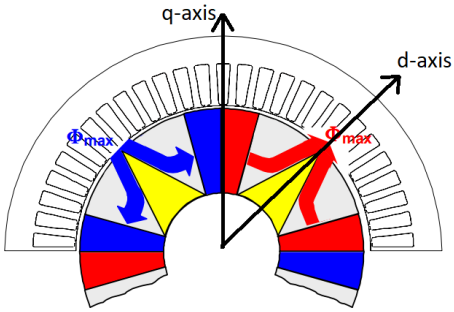

Fig. 6: The first proposed VF-PMSM design. The magnets are of low-coercivity type and tangentially magnetized. Red: North pole. Blue: South pole. Yellow: non-magnetic material. [2]

Assume the machine is initially operating at rated speed with fully magnetized PMs, as depicted in Fig. 6. If the speed is to be increased beyond its rated speed, the induced back-emf in the windings may cause overvoltage if not compensated for. While most PMSM would inject continuous negative d-axis current to suppress the back-emf, this machines can simply send a short current pulse in the negative d-axis to partially demagnetize the PMs. The flux rising from such a pulse is illustrated in Fig. 7a. Due to the trapezoidal shape of the magnets, the flux lines will penetrate the magnets more densely close to the shaft and less so closer to the air gap. The low coercivity allows this flux to partially demagnetize the magnets. After the current pulse, the magnetization distribution is as shown in Fig. 7b. As can be seen, the demagnetizing flux caused the portion of the magnets closest to the shaft to not only demagnetize, but to magnetize in the reverse direction. This allows some of the flux to circulate in the magnets, decreasing the total rotor flux that crosses the air gap. Consequentially, the back-emf induced in the windings is now lower for a given speed, allowing operation above the rated speed without risking overvoltage. In terms of Eq. 4, λ_{fd} is decreased, causing v_{sq} and the terminal voltage to decrease as well.

Once the machine is to return to a high-torque, low-speed operating point, a positive d-axis current pulse can be injected to re-magnetize the PMs so as to supply maximum flux.

The advantage of VF-PMSMs is not only that it allows high-speed operation with less copper losses due to flux weakening current, but also that it can maintain high efficiency across a large space of torque/speed operating points. The control system can be made to estimate the air gap flux that will result in the lowest losses for a given operating point. Based on this estimation, the rotor magnets can be partially demagnetized or re-magnetized to maximize efficiency at that operating point, simply through a brief d-axis current injection.

After the VF-PMSM was introduced, the idea did not initially attract much attention. This was possibly due to the

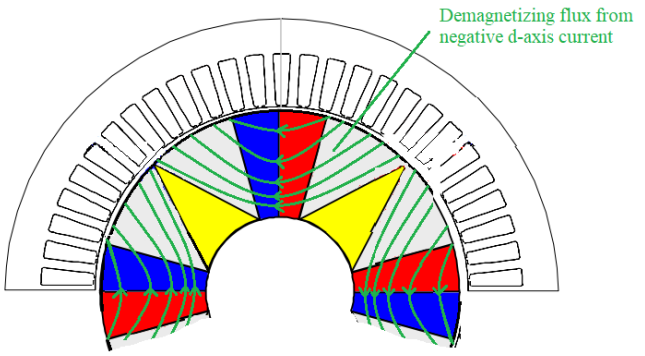

(a) Demagnetizing flux lines.

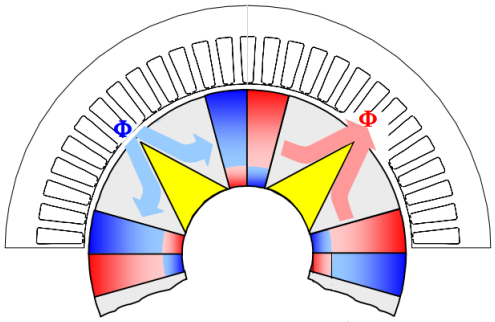

(b) Resulting magnetization state of PMs.

Fig. 7: Controlled demagnetization of the VF-PMSM in [2].

difficulty of making a control system that can reliably achieve the optimal magnetization level for any operating point. This is challenging because the amount of d-axis current injection needed to give just the right amount of demagnetization or re-magnetization is difficult to estimate accurately. Successful efficiency maximization in a VF-PMSM has several dependencies, such as precise estimation of the present magnetization state, compensation for temperature effects on the BH-curve, and adequate inverter rating. In recent years, researches have started to overcome these difficulties and have demonstrated significant loss reduction through active control of PM magnetization.

VI. VF-PMSM Designs

During the last few years, several new VF-PMSM designs have been proposed. Some are just slightly changed versions of the original design in [2], while others are completely different.

In [2], the design shown in Fig. 6 was only tested using ferrite magnets as the PM material. As mentioned earlier, ferrite (ceramic) magnets have low remanent flux compared to other PM materials. As such, the paper concludes that better performance could be achieved if AlNiCo were used instead. After this original VF-PMSM, ferrite magnets has almost never been used in such designs. In most designs, either AlNiCo or a soft SmCo grade is used as the low-coercive magnet material.

A. Improvements to the Original Design

In [9], a design similar to the original memory motor is optimized to improve torque quality and reduce the current required to re-magnetize the PMs. The final design is shown in Fig. 8, including the flux density distribution at full magnetization.

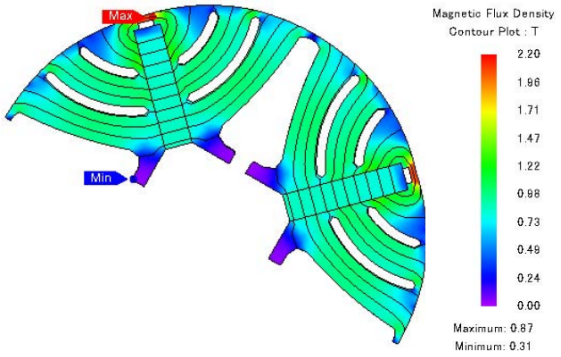

Fig. 8: Rotor design and flux density distribution at full magnetization in an improved VF-PMSM using AlNiCo magnets. [9]

In this improved design, the main difference from the original VF-PMSM design is the rectangular (rather than trapezoidal) shape of the magnets, and the additional flux barriers. The researches found, through finite element simulations, that this design achieved higher torque density, less torque ripple and lower magnetization current.

This machine topology has also been thoroughly investigated in [10]–[14]. In [14], specific rotor parameters (dimensions and position of magnets and flux barriers) were optimized using the Genetic algorithm to minimize torque ripple and magnetization current. This design is one of few VF-PMSM designs that has been optimized and has an associated vector control system with proven functionality. The control system will be reviewed in section VII.

B. Other Single-Material PM Designs

Recently, a model based design methodology for VF-PMSMs using only one magnet material was presented in [15]. The general topology on which the model is based is shown in Fig. 9.

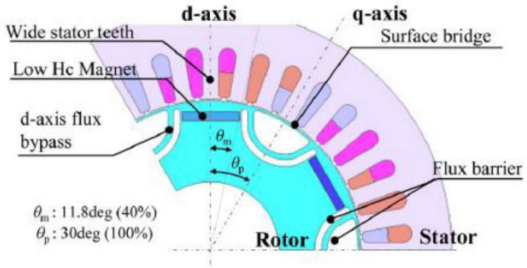

Fig. 9: Base model for the design methodology proposed in [15].

Based on input constraints such as outer radius, stacking length, magnet material properties, target magnetization state, max phase current, current density of stator slot, and max

flux density of iron core, the model will give a solution space of possible magnet widths and thicknesses that fit the input criteria. The model can then be used to find the torque and power factor for any viable combination of magnet width and lengths, allowing the machine designer to chose dimensions according to individual priorities of torque and power factor. The model also provides the margin to the demagnetization limit, i.e. how close the maximum load current will be to cause uncontrolled demagnetization of the PMs.

C. Using High-Coercivity Magnets in Parallel

Many other suggested designs are based on the idea of using magnets with high coercivity in parallel or in series with the low-coercive magnets. This way, higher air gap flux can be achieved, while maintaining some, albeit often reduced, range in which the rotor flux level can be controlled. Several such designs are reviewed in [16]. Four of them are shown in Fig. 10.

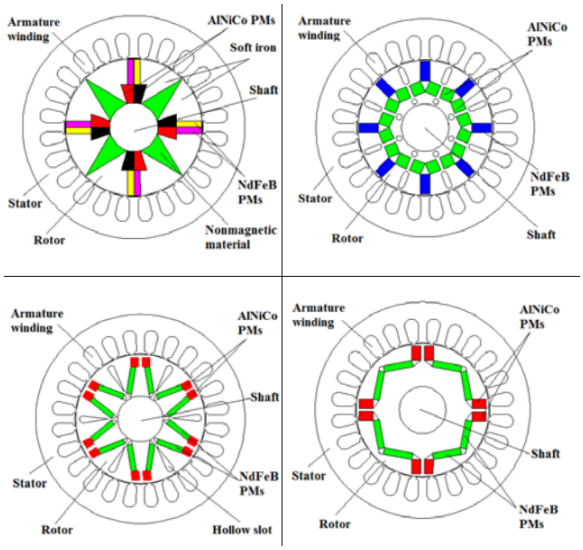

Fig. 10: VF-PMSM designs utilizing high-coercive NdFeB PMs in parallel with AlNiCo PMs. [16]

The idea behind each of the configurations in Fig. 10 is the same. The AlNiCo magnets are placed such that injected d-axis current will cause flux to go through the AlNiCo magnets and change the magnetization. Meanwhile, the magnetization of the high-coercive NdFeB is constant. In these designs, the AlNiCo will not only vary in magnetization level, but also in magnetization *direction*. When the AlNiCo north poles are facing the NdFeB north poles, the air gap flux is boosted, becoming the sum of the fluxes from both magnet types. When the AlNiCo is magnetized so as to have its north poles facing the NdFeB south poles, however, some of the magnet flux is "short-circuited", circulating in the rotor. This weakens the air gap flux. As such, controllable air gap flux is achieved through d-axis current pulse injections.

Though the idea of designs like this may seem promising, [16] concludes that they often require too high magnetization current, have unstable characteristics under operation and have only been tested in no-load operation. Complete, functioning vector control systems are rarely reported.

Still, there is one design using AlNiCo and NdFeB in parallel that has been demonstrated to function in loaded operation [17]. This design is shown in Fig. 11.

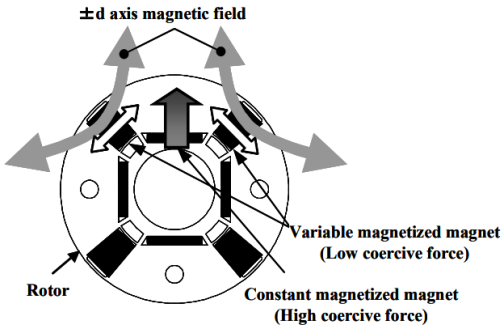

Fig. 11: VF-PMSM design utilizing high-coercive NdFeB PMs in parallel with AlNiCo PMs. [17]

This configuration utilizes the same mechanism as described above for other parallel-magnets rotor designs. The flux lines and air gap flux density distribution at maximum positive magnetization and at maximum negative magnetization is shown in Fig. 12 and Fig. 13, respectively.

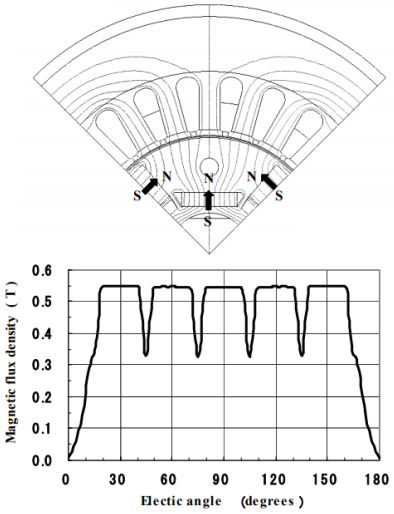

Fig. 12: Flux distribution at maximum positive magnetization of the low-coercive magnets. [17]

The ability of this machine to achieve magnetization change while on load was confirmed experimentally in [17]. However, as can be seen in Fig. 12, the maximum air gap flux is 0.55 T, which for many applications will be too low. Furthermore, a reliable control system that can achieve loss reduction at arbitrary operating points has not been developed for this design. As such, its practicality is limited.

Another parallel-magnets rotor configuration was investigated in [18]. The general topology is shown in Fig. 14.

If the three magnets have the same thickness, the equivalent magnetization of one pole in this topology is given by

$$J_e = \frac{J_l m w_l + J_h m w_h}{m w_l + m w_h} \tag{7}$$

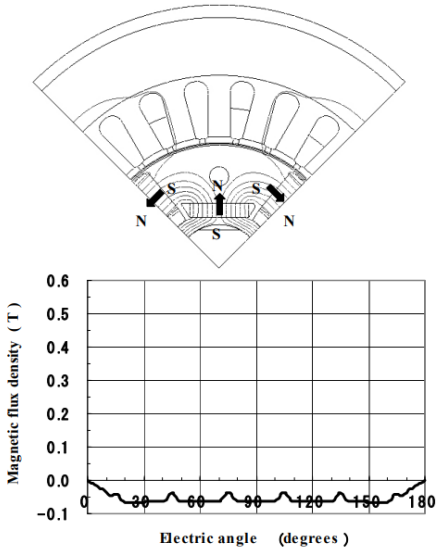

Fig. 13: Flux distribution at maximum negative magnetization of the low-coercive magnets. [17]

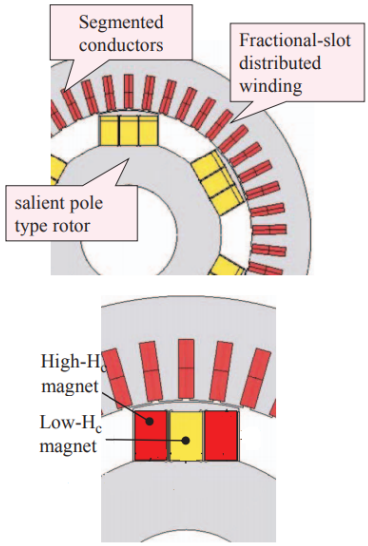

Fig. 14: VF-PMSM topology with high- and low-coercive magnets in parallel. [18]

where J_l and J_h is the magnetization of the low- and high-coercive magnets, respectively. mw_l and mw_h is the width of the low- and high-coercive magnets, respectively.

In [18], a differential evolution based genetic algorithm was implemented to find the specific magnet dimensions in Fig. 14 that maximizes torque density and power capability while maintaining a sufficiently large magnetization control range. With these constraints, the optimal solution was found to use 64.7% high-coercive magnets, in terms of the total magnet width.

D. Using High-Coercivity Magnets in Series

In addition to optimizing the parallel configuration, [18] also runs the genetic algorithm to find the optimal magnet dimensions in a similar overall machine topology using series-connected magnets rather than parallel. The stator and rotor is similar to that shown in Fig. 14, except that the magnets now are configured as shown in Fig. 15.

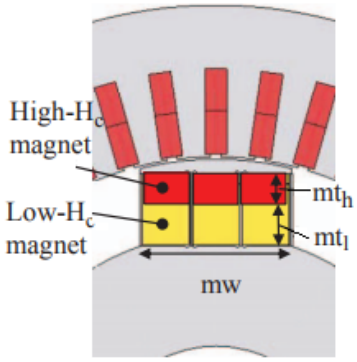

Fig. 15: VF-PMSM topology with high- and low-coercive magnets in series. [18]

When the width of both magnet types are equal, the equivalent magnetization of one pole becomes

$$J_e = \frac{J_l mt_l + J_h mt_h}{mt_l + mt_h} \tag{8}$$

where mt_l and mt_h is the thickness of the low- and high-coercive magnets respectively.

With this magnet configuration, the optimization algorithm found that best performance would be achieved with the high-coercive magnet material taking up 16.5% of the total magnet thickness.

The performance of the series configuration in Fig. 15 and the parallel configuration in Fig. 14 will be compared in Section VIII.

E. Stator design for VF-PMSM

In general, the stator does not need to be designed in a special manner in VF-PMSMs. As long as current vector control is possible, changing magnetization of the PMs is also possible. However, some slot numbers and winding configurations can be preferable in terms of the amount of stator current required for a magnetization change. During magnetization change, the stator steel is often saturated, so most of the mmf dissipates over the stator reluctance. According to [11], the slot number can significantly affect this phenomenon.

[11] investigates, through FE simulations, the effect of slot number on the performance of a VF-PMSM with tangentially magnetization AlNiCo, such as the one shown in 8. The results are given in Table I.

TABLE I: Effects of slot number on a three-phase, 6-pole VF-PMSM. [10]

	Integral			Fractional	
	18 slots	36 slots	54 slots	9 slots	27 slots
Slots/pole	3	6	9	1.5	4.5
Winding factor	1	0.966	0.960	0.866	0.945
Torque ripple %	117	27	18.6	110.1	12.5
Efficiency %	94.6	94.7	94.7	93.8	94.8
Magnetization current (A)	23.6	33.0	33.5	20.61	30.25

Though a low slot number require less magnetization current, it also gives substantially higher torque ripple. For the 6-pole AlNiCo design, a fractional winding with 27 slots, i.e. $q = 1.5$ slots per pole per phase, is chosen as a compromise between torque and magnetization current. [10]

The optimized series configuration in Fig. 15, one of the most researched and best performing VF-PMSM designs to date, uses a stator with $q = 2.5$. [18]

VII. The Design Process

A. The stator

Since VF-PMSMs do not pose absolute restrictions on the stator, as discussed above, the designs developed here use a stator originally built as part of an induction machine. Using a pre-made stator saves significant time and money, and allows the shifting of focus to the most significant part of a VF-PMSM: the rotor. As such, this project is limited to the design of VF-PMSM rotors fitting the geometry of this stator. The ratings of the original induction machine are shown in Table II, while stator geometry and winding configurations are given in Table III.

TABLE II: Specifications of the induction motor whose stator is reused in the VF-PMSM designs.

Symbol	Parameter	Value
P_n	Power	11kW
U_n	Voltage	400V
I_n	Current	21.8A
P	Poles	4
η	Efficiency[1]	88.8-81.7%
n_n	RPM	1460
cosØ	Power factor[1]	0.84-58

TABLE III: Stator geometry and winding specifications.

Symbol	Parameter	Value	Measure
R_{so}	Stator outer radius	130.5	mm
R_{sb}	Stator back radius	105	mm
R_{si}	Stator inner radius	85	mm
W_s	Slot opening	3.5	mm
W_{si}	Slot width inside shoe	7.68	mm
W_{sb}	Slot bottom width	10.83	mm
W_t	Tooth + shoe width	11.3	mm
W_{bi}	Back iron width	25.5	mm
W_{tb}	Tooth width	7.5	mm
d_1	Shoe depth	1	mm
d_2	Shoe depth	1	mm
d_3	Slot conductor depth	18	mm
d_s	Total slot depth	20	mm
L	Active length	137	mm
k_s	Stacking factor	0.97	
	Winding parameters		
n_s	Number of turns per coil	17	
	Parallel strands	3	
N_s	Number of slots	36	
q	Slots per pole and phase	3	
τ_c	Coil pitch	8	Slots
τ_p	Pole pitch	9	Slots
T_{ph}	Turns pr phase	102	
k_w	Winding factor	0.9306	
τ_s	Angular slot pitch	10	Degrees
A_s	Slot area	1.74	cm^2

B. Choice of rotor magnets

The rotor designs reviewed in Section VI can be divided into four distinct categories according to which magnets are used and how they are configured: those using a low-coercive force (LCF), azimuthally magnetized material as the only magnet material on the rotor (Fig. 8); those using only radially magnetized LCF magnets (Fig. 9); those using high-coercive force (HCF) and LCF magnets in parallel (Fig. 10); and those using HCF and LCF magnets in series (Fig. 15).

Originally, the plan was to build a rotor from each of these categories and and compare experimental results. However, after having contacted several magnet providers, it was proven difficult to find appropriate magnets. Specifically AlNiCo magnets, being the most common magnet material in VF-PMSMs, would have had to be custom made to fit with any of the common rotor topologies. Since this project is restricted with respect to both time and money, having magnets custom made is not an option. As such, VF-PMSM designs using AlNiCo magnets are not further investigated here.

Since significant advances have recently been made with designs using a combination of high-coercive NdFeB magnets and low-coercive SmCo magnets [5], and since these materials are readily available on the market, the design process will be limited to SmCo and NdFeB magnets.

C. Designing the rotor topologies: round one

A design methodology for combining SmCo and NdFeB magnets in VF-PMSMs has been developed in [18]. There, both parallel and series configurations were investigated and optimized. However, only the series configured design was built and tested, while the parallel design remains merely simulated. Since there is a lack of literature on SmCo-NdFeB parallel designs, this will be the basis for one of the rotor designs built here.

To limit the cost of the project, it was decided that only two rotor designs should be developed and built. Since there is also a lack of publications on VF-PMSMs using SmCo as the sole magnet material, this will be the other design investigated here.

In order to find the impact of having constant magnetization HCF magnets in parallel with the variable magnetization LCF magnets, the two rotors will be built with identical topology, except for the magnet arrangement. This way, the parallel configured HCF magnets' effect on back-emf and magnetization control capabilities should be clear by comparing the experimental results of the two rotors, avoiding variation due to other factors such as unequal saliency or magnet pitch.

Using the optimized design from [18] as a basis, the first draft of the rotor topology was made and is shown in Fig. 16.

The q-axis flux barriers in Fig. 16 serve to focus the flux from the stator d-axis current to go through the magnets during magnetization. This rotor saliency is critical for the operation of VF-PMSMs, and is exploited in almost all published designs. The shape of the flux barriers in Figure 16 is made to roughly resemble those of [18], but an exact formation is not critical for the purposes of this investigation.

The overall rotor topology is, as mentioned, similar for both rotors designed here. The magnets, however, will be different.

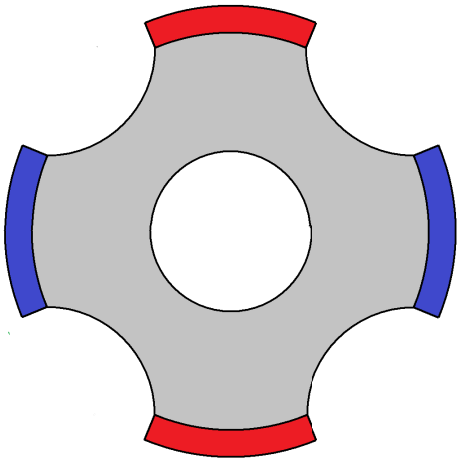

Fig. 16: First draft of the overall rotor design.

Using the optimized parallel configuration from [18], the first draft magnet layouts of a single pole, is shown in Fig. 17.

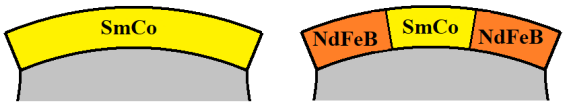

Fig. 17: Magnet layouts of the first draft rotor designs.

D. Magnet specifications

Having the first draft as a basis, several magnet suppliers were contacted and asked for magnets with fitting characteristics and size to fit the draft topology. With a short time frame and a budget limited to 10000 NOK the magnets could not be custom made for the purpose of this project. Finding appropriate off the shelf SmCo magnets proved difficult, mainly due to the desire of a low intrinsic coercivity to facilitate the magnetization process. High-coercivity NdFeB, on the other hand, was readily available.

The specifications and dimensions of the magnets that were finally chosen as a compromise between size, price, delivery time and magnetization characteristics are shown in Fig. 18 and Table IV.

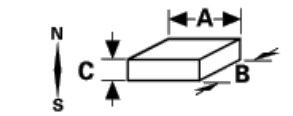

A	x	B	x	C
10,0	x	10,0	x	3,0

Fig. 18: Magnet dimensions. Values given in millimeters. Equal for both NdFeB and SmCo.

Note that the magnetization behavior of this SmCo grade is not quite similar to the general SmCo curve displayed in Fig. 4. The most significant difference is the high intrinsic coercivity, making the second quadrant BH-curve more similar to the curve drawn for NdFeB, with a knee point below the H-axis.

TABLE IV: Magnetization specifications for the permanent magnets used in the designs.

Magnetic values	Energy product (BxH)max	Remanence Br	Coercive field strength (T = 20°C)		Max. working temperature *
			$_BH_C$	$_JH_C$	
	kJ/m³	mT	kA/m	kA/m	°C
Sm_2Co_{17} (190/119)	≥ 190	≥ 1000	≥ 680	≥ 1195	= 300
NdFeB (262/135)	262-288	1170-1250	>860	>1350	120

E. Designing the rotor topologies: round two

In the first draft, the air gap length was not specified since this was only to serve as a rough foundation on which to base the design process. However, now that the magnets are known to be 3 mm thick, the total air gap length was set to 5 mm, giving a 2 mm margin between magnets and stator. As such, with an inner stator radius of 90 mm, the rotor iron diameter becomes 80 mm. This is not ideal in terms of performance, since the flux density of the magnets would have been higher with a smaller air gap. However, in this project, making the manufacturing easy and is prioritized over performance.

To fit the exact dimensions of the chosen magnets, certain alterations must be made to the rotor designs. Given the size and shape of the magnets it was found that to best resemble the first draft, each pole should consist of five separate magnets. For the parallel NdFeB-SmCo design, the three middle magnets should be SmCo, while the two outermost magnets on each pole should be NdFeB. The magnet layout for the pure SmCo design is identical, except, obviously, that all five magnets are SmCo.

To facilitate the attachment of the magnets to the rotor, the poles were designed with five distinct flats, rather the the single arc as in the first draft. With the magnets being 10 mm wide, the flat width were set to 11 mm, allowing some margin between each magnet. The purpose of this is to make the gluing process of the rectangular magnets easier.

Since the active length of the stator is 137 mm and the magnets are 10 mm long, the magnets cannot cover the full length. Thirteen magnets will be attached along the axial length of the rotor, leaving 7 mm uncovered. This will slightly decrease the performance of the machine, but should be inconsequential for the purposes of this project.

A further design change at this stage was made to the q-axis flux barriers. To make manufacturing cheaper and quicker, the flux barriers were changed from circular to rectangular. The depth of these were set to 15 mm, which should be enough to make the rotor significantly salient, while preventing magnetic saturation of the rotor iron under the poles, where the d-axis flux path is at its thinnest.

F. Designing the rotor topologies: round three

Once the manufacturing of the rotor was about to start, another limitation was elucidated; due to the nature of the manufacturing tools, the flats on which the magnets were to be mounted had to have a width such that 360° divided by the angle between two flats equals an integer. In terms of Fig. 19, 360° divided by θ must be an integer. With the original flat width of 11 mm, θ becomes 8.14°, not fulfilling the requirement. 1 mm margin for each magnet was considered somewhat excessive, leading to the decision of decreasing the flat width to the closest allowed value, rather than increasing

it. The closest allowed value for θ below 8.14°, is 7.5°, making the flat width 10.41 mm.

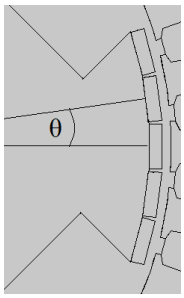

Fig. 19: The angle θ between two flats is restricted by the manufacturing method.

Slightly changing the flat widths will affect other lengths of the rotor as well. The final rotor design is shown in Fig. 20. A photograph of the rotors (before the magnets were attached) along with the stator is shown in Fig. 21.

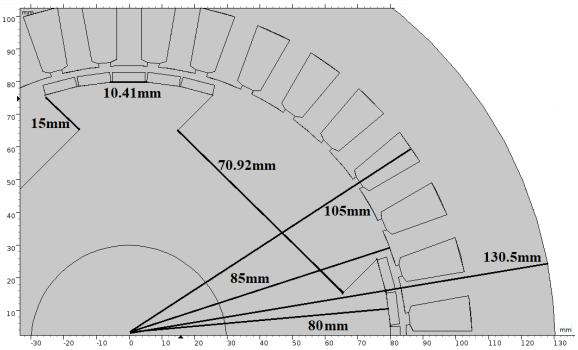

Fig. 20: Final machine topology

Fig. 21: Photograph of the stator and rotors before magnets were attached.

VIII. Experimental Procedure

The most advanced VF-PMSMs found in literature use complex control systems to change the magnetization of the rotor magnets while the machine is operating under loaded conditions [12] [19] [20]. This has been, and continues to be, perhaps the biggest technical challenge of VF-PMSMs. In this project, however, the goal is not to demonstrate the performance or loss reducing capability of a VF-PMSM. Instead, the aim is simply to investigate the degree to which magnetization change through stator current injection is possible. As such, a complex control system is not necessary in these experiments.

Most VF-PMSMs use control systems that track the position of the moving rotor and inject appropriate current pulses in the rotating d-axis to achieve magnetization change. For simplicity, this project will instead attempt magnetization change under stationary, no-load conditions. When the rotor is stationary, magnetization change can be achieved simply by the injection of a DC stator current, negating the difficulties of a control system.

Details on the various instruments and circuit components described in this section can be found in Appendix B. Photographs of the experimental setup are shown in Appendix C.

Unfortunately, due to unforeseen challenges in the laboratory, time did not allow the testing of both designs. As such, the rest of this paper will solely be concerned with the rotor having only SmCo magnets.

A. Aligning the rotor

For the desired demagnetization or remagnetization to take effect, the direct current in the stator must be distributed such that it creates a magnetic field in the direction of the rotor d-axis. To ensure that the rotor magnets are aligned with the stator magnetization field, a small direct current can be injected into the stator before the magnetization pulse. If the rotor field is not parallel with the resulting stationary stator field, an electromagnetic torque will move the rotor into alignment. Note that this technique would work even if the permanent magnets were completely demagnetized, due to the salient nature of the rotor. The amount of stator current necessary to ensure rotor alignment is much lower than the magnetization current pulses and will not be able to affect the magnetization levels of the PMs. In this experiment, short current injections of 8 A were used to move the rotor into magnetization position.

Throughout the experiment, the stator phases are Y-connected. When injecting alignment current or magnetization current, one phase is connected to a given pole of the source while the two other phases are both connected to the opposite pole. For a given DC stator current injection, then, the phase currents will be as shown in Figure 22.

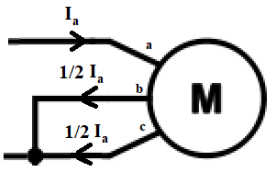

Fig. 22: Phase currents during injection of alignment current and magnetization current.

B. Magnetization current

In order to investigate the effect of magnetization current on the magnetization state of the rotor magnets, an external

circuit that can provide magnetization currents of various levels is needed. Ideally, this current source should be a DC current source that can pulse the stator with exact, predefined levels of magnetization current up to a few hundred ampere. Unfortunately, such a source was not available for this project. Instead, a capacitor bank was used to provide magnetization current.

Once the rotor is properly aligned, as described above, the magnetization process can commence. First, a variable DC source (rated to 400 V, 1 A max) is used to charge up the capacitors to a given voltage level. Afterwards, the DC source is disconnected from the capacitor bank which is subsequently connected to the stator windings, through a thyristor switch. Due to the low impedance of the machine, the capacitors are rapidly discharged once connected to the stator windings, and a magnetization current pulse arises .

For remagnetization to take place, the magnetization current must follow the same path through the stator as the alignment current did. This means that if, for example, the alignment current enters into phase a and returns through phase b and c (as in Figure 22), then the remagnetization current must do the same. For demagnetization, on the other hand, the current direction must be reversed, so that the resulting stator field opposes the permanent magnets and, with a sufficient amount of current, lowers the magnetization state of the magnets.

The magnetization current resulting from the capacitor bank discharge will depend on the voltage to which the capacitors were charged. As such, the magnetization current can be indirectly controlled by charging the capacitors to a variety of voltages. The full magnetization circuit is displayed in Figure 23. The free-wheeling diode connected between the terminals serves as a fail-safe in case the current is cut, potentially resulting in a damaging overvoltage due to the inductive nature of the machine.

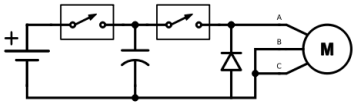

Fig. 23: The circuit used to inject the magnetization current.

Figure 24 shows the measured stator terminal voltage and current curves as the charged capacitor bank is switched in. In this case, the capacitor bank was charged to 280 V, resulting in a peak demagnetization current of 178 A.

C. Estimating the magnetization state

Since the magnets are mounted inside the machine when the magnetization change takes place, there is no easy access to accurately measure the magnetization state of the magnets. However, since the no-load back-emf induced at a given rotor speed is proportional to the air-gap flux, this can be used as an estimator for the MS of the magnets.

No-load back-emf is found by first connecting the shaft of the VF-PMSM to a fully controllable DC-motor. While the terminals of the VF-PMSM are open-circuited, the other machine is used to accelerate the motors to 1500 rpm, giving a back-emf with rated frequency of 50 Hz. The resulting back-emf is

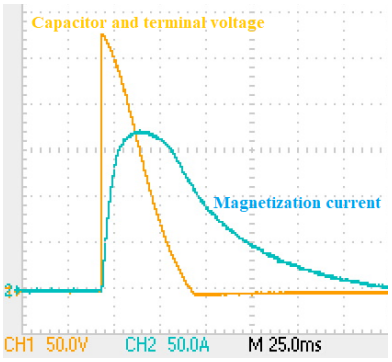

Fig. 24: Terminal voltage and magnetization current as the charged capacitor bank is connected to the stator terminals.

measured by two instruments: an oscilloscope and a voltmeter. Three different back-emf measurements can be used as the MS estimator: rms back-emf as measured by the voltmeter, rms back-emf as measured by the oscilloscope, and peak-to-peak back-emf as measured by the oscilloscope. Before the fully magnetized magnets were attempted demagnetized, several test-measurements of back-emf were carried out, recording all of the three aforementioned values, while keeping the magnetization state constant (no injection of magnetization current). It was found that the voltmeter-measured rms back-emf was most reliable in terms of uncertainty. Thus, this is the measurement that is chosen to estimate magnetization state. Still, all three back-emf measurements are recorded throughout the experiment.

Figure 25 shows the initial back-emf curve along with the corresponding voltage measurements. When these measurements were done, no magnetization current had yet been injected into the stator. As such, these numbers represent the full magnetization level at which the magnets were shipped. All subsequent MS estimations will be given in percentage of this baseline value.

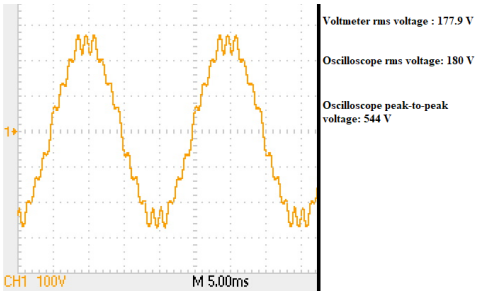

Fig. 25: Back-emf voltage induced between two phases of the stator at 1500 rpm at full magnetization

IX. Theoretical Calculations and Finite Element Analysis

With an established design and experimental approach, it is possible to make theoretical calculations to which the experimental results can be compared. Furthermore, a simple finite element model of the machine can be used to confirm the derived calculations and facilitate more detailed analysis.

Since precise magnetization curves are not given for the SmCo magnets used here, an accurate theoretical description of the machine's magnetization behavior cannot be established easily. However, the minimum values provided in Table IV can be used to give an indication of how the magnets will be affected by a given magnetization current.

A. Theoretical Calculation of Magnetization Currents and Fields

In addition to being affected by the magnetization field, the permanent magnets are also subject to an opposing load field due to the air gap. With the magnets occupying 3 mm of the 5 mm air gap (neglecting variation due to stator teeth and rectangular magnet shape), the load field becomes

$$H_l = \frac{2\ mm}{5\ mm}\frac{B_r}{\mu_0} = 318\ \frac{kA}{m} \tag{9}$$

where B_r is the remanence of the magnets. Correspondingly, the magnets will provide an air gap flux density of

$$B = \frac{3\ mm}{5\ mm}B_r = 0.6\ T. \tag{10}$$

The total field in the magnets is

$$H = H_l + H_m \tag{11}$$

where Hl is the load field and Hm is the magnetization field.

A simplified relationship between magnetization current and the resulting magnetization field acting on the magnets can be found using

$$Hl = NI \tag{12}$$

where H is the magnetic field, l is the air gap length, N is the number of turns and I is the current. To illustrate how this equation can be applied to the topical machine, Figure 26 shows how the magnetization current is distributed over a pole during the magnetization process. Since several of the stator slots lie within the magnet pitch, the magnetization field will vary throughout the magnets. Even though the b-phase turns and the c-phase turns within the pole pitch in Fig. 26 are not physically part of the same coil, they can be considered as such when Eq. 12 is used.

Since only the middle magnet is placed such that it lies within all the coils, its location will serve as the reference point in the following calculations. It should be noted, though, that the field strength acting on the other magnets will be weaker, as these do not "link" with all the ampere-turns of the pole.

With the phases connected as shown in Fig. 22, the ampere-turns linked at the reference point inside the middle magnet become

$$NI = N_a I_a + N_{bc}\frac{1}{2}I_a \tag{13}$$

where N_a is the number of a-phase turns within the pole, N_{bc} is the number of turns in the three virtual coils consisting of the b-phase slots and the c-phase slots. Using 17 turns per coil and changing phase a current with magnetization current further yields

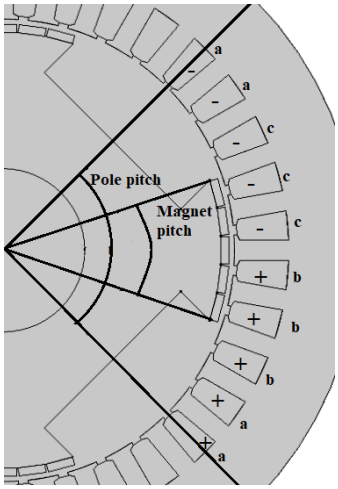

Fig. 26: Magnetization current distribution in the phases within a pole. + and - indicates direction of current (out of plane and into plane, respectively).

$$NI = (1.5 + 3 \cdot \frac{1}{2})17I_m = 51I_m \tag{14}$$

The resulting magnetization field is then

$$H_m = \frac{76.5I_m}{l} = \frac{51I_m}{5\ mm} = 10200I_m \quad [A/m] \tag{15}$$

So according to Eq. 15, every ampere increase in magnetization current will give a 10.2 kA/m increase in magnetization field.

Using Eq. 15 and assuming the minimum intrinsic coercivity in Table IV, the magnetization current required to completely demagnetize the magnets becomes

$$I_m = \frac{H_{jc}}{10200} = \frac{1195}{10.2} = 117.2\ A. \tag{16}$$

Here, the load field is not included since by the time the magnet is completely demagnetized, the load field is zero. Assuming a constant load field is only valid for small magnetization changes.

Magnetization currents lower than 117.2 A, then, will only cause partial demagnetization or - if it is too small - no demagnetization at all.

Predicting exactly at which current level partial demagnetization starts is difficult given the lack of an accurate magnetization curve for the permanent magnets. However, to facilitate the discussion, an approximate magnetization curve can be drawn by using the magnet characteristics in Table IV and the typical shape of a SmCo magnetization curve. Such an approximated curve is displayed in Figure 27, showing both the intrinsic and the normal magnetization curves.

Partial demagnetization then occurs for field strengths between the point at which the intrinsic curve start dropping (the knee point) and the intrinsic coercive strength (where the intrinsic curve reaches zero, H_{jc}). The remagnetization

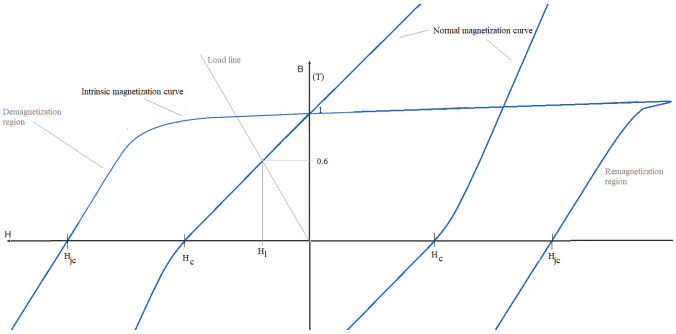

Fig. 27: Approximated magnetization curves of the SmCo magnets, based on the values in Table IV.

process is more demanding, as this occurs along the rightmost line of the intrinsic curve in Figure 27. The entire remagnetization region lies above the intrinsic coercivity, meaning that the magnetization current required for remagnetization will always be higher than that needed for demagnetization. Remagnetization is made even harder due to the fact that the load field acts in the opposite direction. While the load field contributes to demagnetization, it opposes remagnetization. The slope of the remagnetization line is unknown and hard to approximate. A lower limit to the magnetization current needed for remagnetization to occur can, however, be calculated using the intrinsic coercivity and the relationship derived in Eq. 15:

$$I_m > \frac{H_{jc} + H_l}{10200}. \tag{17}$$

Here, H_l is the load field *post* magnetization, depending on the level to which the magnets are brought. When establishing a lower bound for the remagnetization current, this load field might as well be set to zero. Thus, the lower bound for remagnetization current becomes equal to the upper bound for demagnetization (Eq. 16):

$$I_m > \frac{H_{jc}}{10200} = 117.2\ A \tag{18}$$

As such, the magnetization current must at least be higher than 117.2 A to cause remagnetization. More precisely, if the magnets were completely demagnetized, 117.2 A would be the level of magnetization current at which the magnets would start to magnetize.

B. Finite Element Analysis

A simple two-dimensional, stationary FE model of the machine was made, based on the stator specifications in Tables III and II and magnet specification in Table IV (using the given minimum values). Note that this project is not mainly focused on FE modelling and thus the scope of this analysis is limited to simple field calculations to confirm the theoretical calculations derived above.

Figure 28 shows the magnetic flux distribution in the machine when no current is flowing in the stator. As expected, the air gap flux density in the region occupied by magnets is approximately 0.6 T.

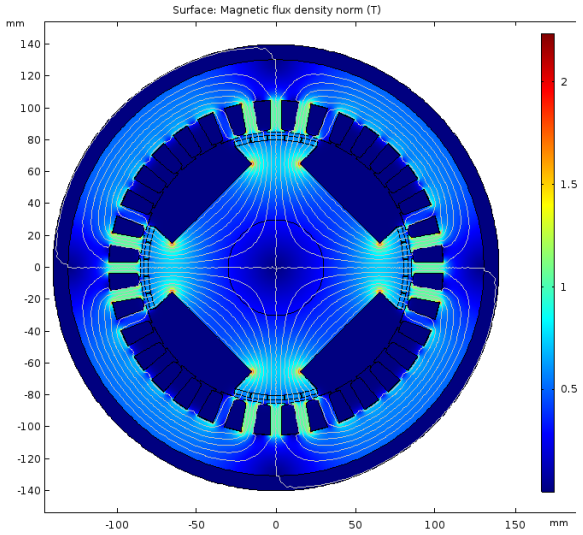

Fig. 28: No-load flux distribution in the manufactured machine at full magnetization.

To investigate the magnetic field acting on the magnets, Fig. 29 shows the magnetic field strength along the displayed arc, cutting approximately in the middle of the magnets. Eq. 9 predicted a no-load load field of 318 kA/m. Fig. 29 confirms this, showing that field fluctuating close to this value. The fluctuations are likely due to the slot openings and slits of air between the magnets.

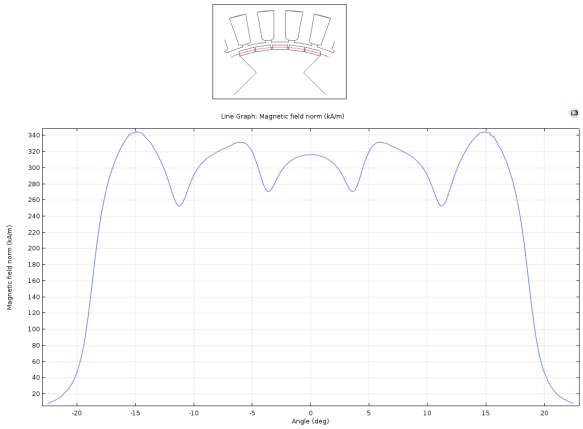

Fig. 29: No-load field distribution along the highlighted arc.

Applying a demagnetization current of 117.2 A, which according to Equation 16 should give a field equal to the intrinsic coercivity of 1195 kA/m, yields the magnetic field distribution (over the same arc as in Fig. 29) shown in Fig. 30.

In Fig. 30, the unevenly distributed field across the magnet pitch due to the variation of linked ampere-turns, as predicted above, is evident. Still, the derived equations should be accurate for the middle magnet. Yet, Fig. 3 shows that the field in the middle magnet is approximately 1500 kA/m, not 1195 kA/m, as predicted. This is due to the fact that the FE simulation is stationary, implying that the magnetization state of the magnets will not change, regardless of how strong the field is. The discrepancy between the simulated and the calculated field, then, is mainly due to the load field

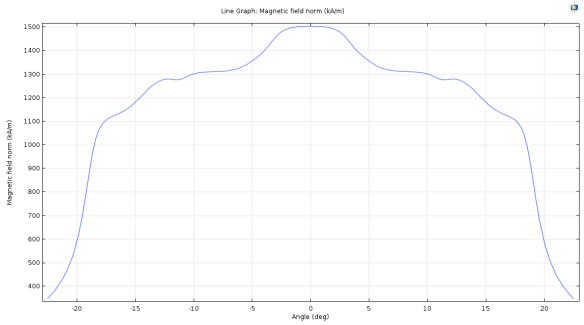

Fig. 30: Magnetic field distribution along the arc highlighted in Fig. 29 during an injection of 117.2 A demagnetization current with fully magnetized magnets.

calculated in Eq. 9. In reality, this load field would have been reduced to zero by the time the field inside the magnets reaches the intrinsic coercivity. Dynamic FE simulation of the magnetization changes is beyond the scope of this paper.

To confirm the validity of Eq. 18 concerning remagnetization, the magnetization of the PMs are set to zero and 117.2 A is injected. The resulting field distribution, again along the arc highlighted in Fig. 29, is shown in Fig. 31.

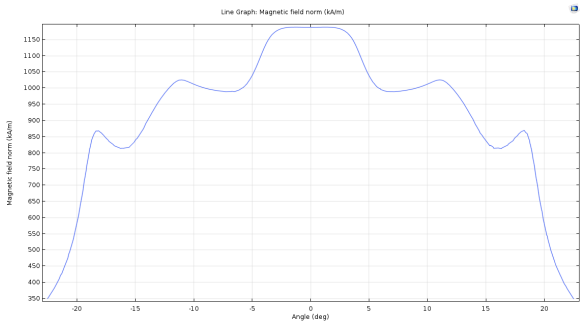

Fig. 31: Magnetic field distribution along the arc highlighted in Fig. 29 during an injection of 117.2 A remagnetization current with zero magnetization in the PMs.

As expected, the field inside the middle magnet is approximately equal to the intrinsic coercive strength of 1195 kA/m, being just on the verge of magnetizing the magnet (see the intrinsic curve in Fig. 27). Moving towards the edges of the pole pitch, however, the field decreases steeply. This means that even if the field is strong enough to magnetize the middle magnet, the other magnets may remain un-magnetized. In advanced VF-PMSMs this issue can be solved by using a control system to move the position of the peak field strength across the full magnet pitch. This way, all magnets reach the same magnetization value. This is possible when the machine is in rotation and the stator current freely controllable. However, with the technique used in this paper, only having a DC magnetization current source and a stand-still rotor, uneven magnetization levels across the magnets is inevitable.

X. Experimental Results

Fig. 32 shows the magnetization states as estimated from measured back-emf rms values, in percentage of the back-emf measured at the initial magnetization level, following an injection of magnetization current. Exact values of all measurements can be found in Appendix A.

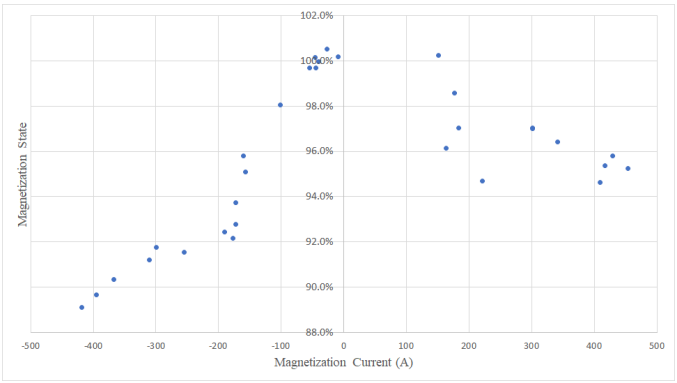

Fig. 32: Measured magnetization states after injection of magnetization current. Negative values are demagnetization currents, while positive values are remagnetization currents.

From Fig. 32 it is clear that the VF-PMSM built in this project does not react to magnetization current in the expected manner. As reported in literature and derived from theory, the data points in Fig. 32 were expected to lie along a curve somewhat similar to the approximated intrinsic magnetization curve in Fig. 27. There are two main aspects of Fig. 32 that seem to deviate from the expected behavior.

Firstly, a significant increase in the magnitude of the magnetizing current (in either direction) should have had a significant impact on the resulting MS of the magnets. The data shows, however, that this is not the case. For example, injecting a demagnetization current of 256 A causes almost exactly the same amount of demagnetization as 368 A does. Moreover, increasing the remagnetization current from 220 A to 416 A had almost no impact on the resulting MS. Note also that the sizes of the injected currents are much larger than what was expected necessary. Eq. 16 predicted 117.2 A to be enough demagnetization current to cause complete demagnetization (at least of the middle magnet). However, the results show that even a demagnetization current as high as 420 A only brought the MS down to 89.2%.

Secondly, the MS to which the magnets are brought by a given magnetization current seem to depend on how low the MS of the magnets have been brought before. More precisely, the lower the magnets have been demagnetized at some point, the easier they are to demagnetize further, and the harder they are to remagnetize back to a given MS. This phenomenon is illustrated in Fig. 33, where the chronological development of the magnetization states are displayed.

As highlighted in the Fig 33, the first successful remagnetization was achieved with a current of 150 A, and brought the MS back to approximately 100%. However, towards the end of the experiment, after repeated de- and remagnetizations, a three times larger current of 452 A, would only bring the MS back up to 95.3%. It seems that once the MS has reached a new all-time low, it cannot return to its former heights, even with the help of significantly higher remagnetization currents.

XI. Discussion of Experimental Results

The experimental results show that magnetization currents of magnitudes far beyond the expected requirements did not cause the anticipated demagnetization or remagnetization.

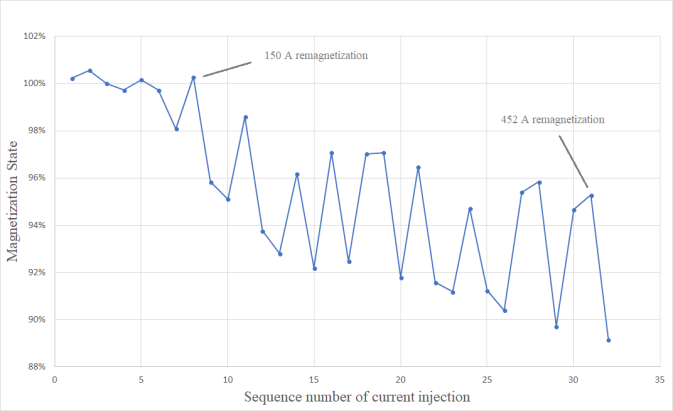

Fig. 33: Chronological development of magnetization state

Since the magnetization field from the injected current should be more than high enough to cause significant magnetization change in the magnets, there must be some parasitic field in addition to the load field and the magnetization field. This tertiary field must oppose magnetization field, neutralizing the effect the magnetization current has on the air gap field.

Through closer post-experimental consideration, it seems likely that this parasitic field can be caused by eddy currents in the rotor. The rotor steel is not laminated, so the induced eddy currents and the ensuing opposing fields during a rapid change in rotor flux can be significant. As can be seen from Fig. 24 the magnetization current is close to its peak value for approximately 30 ms. This means that the rotor steel has a very short time to change its flux before the applied magnetization field dies out. For example, if one applies a demagnetization field of such a size that the sum of the load field and magnetization field is twice that of the coercive strength, then the flux through the magnets must change from 0.6 T to - 1 T. Here it is assumed that no demagnetization occurs *during* the flux change, so that the linear region of the normal magnetization curve in Fig. 27 can be extrapolated down to the applied field. If demagnetization did occur, however, the flux change would be even bigger, as this would imply that the load field decreased. Clearly, magnetization changes requires substantial and rapid changes of the flux, potentially making eddy currents an issue.

Eddy currents are a consequence of the Maxwell-Faraday relation;

$$\nabla \times \boldsymbol{E} = -\frac{\delta \boldsymbol{B}}{\delta t} \tag{19}$$

where $\boldsymbol{E}$ is the electric field and $\boldsymbol{B}$ is the magnetic flux density. In a medium with high conductivity, such as the non-laminated rotor core, a curled electric field will produce a significant circulating current, giving rise to a magnetic field opposing the external field. Consequently, Eq. 19 implies that a rapid change in magnetic flux density in highly conductive media will require a significantly stronger external field compared to a similar change in non-conductive media.

If the current in Fig. 24 is considered a demagnetization current pulse with duration 30 ms, and if the resulting field is twice the coercive strength, then the average time derivative of the magnetic flux in the magnets must at least be

$$\frac{\delta B}{\delta t} > \frac{0.6 - (-1)\ T}{0.03\ s} = 53.3\ T/s \tag{20}$$

for the flux to build up to the required level.

From the experimental results it seems that the opposing eddy current fields are too large to allow such a rapid change in flux. Consequently, the field inside the magnets do not reach the value predicted by Eq. 11 in time before the magnetization field subsides.

The eddy current fields are believed to play a similar role during remagnetization as that described above for demagnetization. However, the change in magnetic field inside the magnets that must take place during remagnetization is larger than that for demagnetization. This implies that the required flux change is also larger during remagnetization. Hence, the eddy currents opposing the change may be even more significant. This asymmetry will increase further once the magnets are partially demagnetized, since the initial flux decreases, increasing the distance to a given remagnetization flux, while moving closer to any demagnetization flux. This phenomenon may explain the graph in Fig. 33; as the magnets are partially demagnetized, they gradually become easier to demagnetize further and harder to remagnetize back to its former magnetization level. After several consecutive de- and remagnetizations, then, the overall magnetization level will decrease, even if the magnitude of the magnetization currents do not change.

To improve the ability to change magnetization in this machine, the most important alteration to make to the experimental setup is probably the magnetization current source. When the only controllable variable is the voltage to which the capacitor bank is charged, it is difficult to achieve the necessary duration of the magnetization current. A source that could provide a specified current for a specified amount of time would be ideal, and could enable more detailed analysis of the machine's magnetization characteristics.

Deriving the minimum duration of the magnetization current required for the necessary flux change to take place is beyond the scope of this paper. However, it seems clear that for VF-PMSMs with non-laminated rotor steel, a long-lasting current injection is needed to achieve proper magnetization change. Since the required magnetization current is often several times larger than the rated current, extending its duration will have detrimental effects on copper losses. If frequent magnetization changes are to take place, the related losses may become so large that they completely negate the loss reduction that the MS changes would have in the first place. After all, the main motivation behind the recent surge in research on VF-PMSM technology is exactly that; loss reduction. As such, laminating the rotor steel is likely a worthwhile investment when designing these machines.

XII. Conclusion

The most important lessons learned in this project can be summarized as follows:

- Finding magnet suppliers that can deliver magnets with magnetization characteristics suitable for VF-PMSMs seems difficult.
- There is a lack of literature on designs using SmCo as the only magnet material.
- Using a capacitor bank as the sole current pulse source is sub-optimal to investigate the magnetization behavior of VF-PMSMs.
- High-coercive SmCo magnets may be inappropriate for this application due to the large current needed to change the magnetization.
- Due to the rapid changes in flux, lamination of the rotor core is essential to achieve magnetization changes using current pulses of reasonable length.
- Not laminating the rotor core may defeat the VF-PMSM's purpose of reducing operational losses.

Appendix A
Measurements

In Fig. 36 measurements of all magnetization current injections are shown. The capacitor voltage is recorded at the moment of connection to the stator windings. The back-emf is measured in three distinct ways; rms voltage as measured by a voltmeter and the oscilloscope, and peak-to-peak voltage as measured from the oscilloscope-recorded curves. Only the voltmeter-measured rms voltage is used to estimate magnetization states. All back-emf voltages are measured between two (star-connected) phases.

		Back-emf at 50Hz (V)		
Capacitor voltage (V)	Peak current (A)	Voltmeter rms	Osc rms	Osc pk-pk
0	0	177.9	180	544
-70	-62.4		182	552
-100	-85.6		179	536
-122	-102	174.5	177	532
-150	-140		178	532
170	150	178.4	182	544
-200	-162	170.5	173	520
-200	-158	169.2	172	516
200	176	175.4	178	536
-230	-174	166.8	169	512
-250	-174	165.1	167	504
200	162	171.1	173	520
-280	-178	164.0	166	504
280	182	172.7	175	528
-300	-192	164.5	166	504
320	>300	172.6	175	528
280	>300	172.7	176	528
-320	<-300	163.3	166	500
280				
280	340	171.6	174	520
-250				
-250	-256	162.9	165	496
-300		162.2	165	496
200	220	168.5	171	516
-300	-312	162.3	165	496
-340	-368	160.8	163	492
340	416	169.7	172	520
340	424			
340	428	170.5	173	520
-360				
-360	-396	159.6	162	488
340	408	168.4	171	512
360	452	169.5	172	516
-380	420	158.6	161	484
	Not measured due to intstrumental or human error			
	Not measured by choice			
	Unreliable measurement (out of instrument range)			

Fig. 34: Capacitor voltage, peak current and subsequent back-emf measurements. Negative values indicate demagnetization.

Appendix B
List of Equipment

- Capacitor bank. 8 parallel connected RIFA PEH200YX4470MU2, 4700 μF, 450 VDC
- Alignment current source. EA-PSI 5200-10 A Power Supply. 200 V, 10 A 640 W
- DC Power Supply for charging of capacitor bank. 2 series connected GW Model GPR-30H10, 300 V, 1 A
- Voltage probe. Tektronix P5200A, 50 MHz
- Current clamp. Fluke i1010
- Oscilloscope. Tektronix TDS2004B
- Voltmeter. Fluke 175 True rms multimeter

Appendix C
Photographs of Experimental Setup

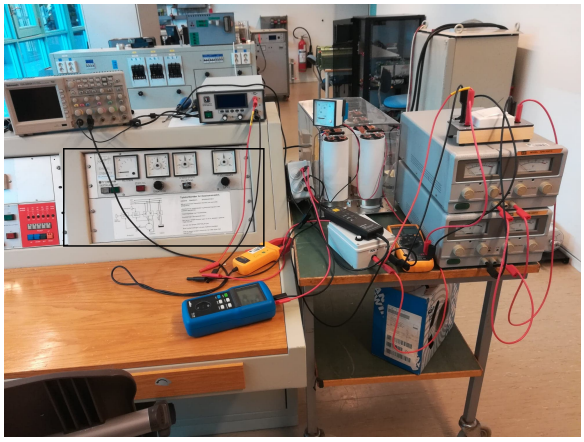

Fig. 35: Magnetization current control circuit and measuring instruments as set up during experiments.

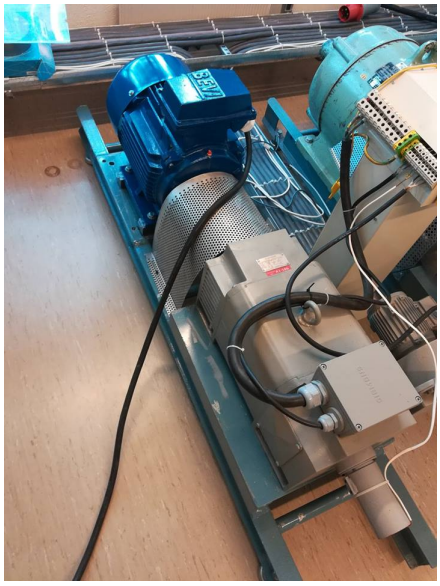

Fig. 36: The tested VF-PMSM (blue) and the DC drive (grey).

REFERENCES

[1] H. Yang, Z. Zhu, H. Lin, and W. Chu, "Flux adjustable permanent magnet machines: A technology status review," *Chinese Journal of Electrical Engineering*, vol. 2, no. 2, pp. 14–30, 2016.

[2] V. Ostovic, "Memory motors-a new class of controllable flux pm machines for a true wide speed operation," in *Industry Applications Conference, 2001. Thirty-Sixth IAS Annual Meeting. Conference Record of the 2001 IEEE*, vol. 4. IEEE, 2001, pp. 2577–2584.

[3] K. Kvinnesland, "Variable flux permanent magnet synchronous machines: A review," Specialization Project, Electric Power Engineering, NTNU, Tech. Rep., 2017.

[4] S. Sjökvist, "Demagnetization and fault simulations of permanent magnet generators," Ph.D. dissertation, Acta Universitatis Upsaliensis, 2016.

[5] H. Yang, H. Lin, and Z. Zhu, "Recent advances in variable flux memory machines for traction applications: A review," *CES Transactions on Electrical Machines and Systems*, vol. 2, no. 1, pp. 34–50, 2018.

[6] "Adams Magnetic Products: Materials Catalog, 2016," https://www.adamsmagnetic.com/sites/default/files/Adams%20Materials%20Catalog%2011_2016.pdf, accessed: 04/12/17.

[7] D. C. Hanselman, *Brushless permanent magnet motor design*. The Writers' Collective, 2003.

[8] N. Mohan, *Advanced Electric Drives: Analysis, Control, and Modeling Using MATLAB/Simulink*. John wiley & sons, 2014.

[9] A. Sun, J. Li, R. Qu, J. Chen, and H. Lu, "Rotor design considerations for a variable-flux flux-intensifying interior permanent magnet machine with improved torque quality and reduced magnetization current," in *Energy Conversion Congress and Exposition (ECCE), 2015 IEEE*. IEEE, 2015, pp. 784–790.

[10] M. Ibrahim, L. Masisi, and P. Pillay, "Design of variable-flux permanent-magnet machines using alnico magnets," *IEEE Transactions on Industry Applications*, vol. 51, no. 6, pp. 4482–4491, 2015.

[11] ——, "Design of variable flux permanent-magnet machine for reduced inverter rating," *IEEE Transactions on Industry Applications*, vol. 51, no. 5, pp. 3666–3674, 2015.

[12] L. Masisi, M. Ibrahim, and P. Pillay, "Control strategy of a variable flux machine using alnico permanent magnets," in *Energy Conversion Congress and Exposition (ECCE), 2015 IEEE*. IEEE, 2015, pp. 5249–5255.

[13] A. Takbash, M. Ibrahim, and P. Pillay, "Torque ripple reduction of a variable flux motor," in *Energy Conversion Congress and Exposition (ECCE), 2016 IEEE*. IEEE, 2016, pp. 1–7.

[14] A. Takbash and P. Pillay, "Design optimization of a new spoke type variable-flux motor using alnico permanent-magnet," in *Electric Machines and Drives Conference (IEMDC), 2017 IEEE International*. IEEE, 2017, pp. 1–6.

[15] K. Sasaki, A. Athavale, B. Gagas, T. Fukushige, T. Kato, and R. Lorenz, "A model based design methodology for variable flux pmsms to obtain desired speed-torque characteristics," SAE Technical Paper, Tech. Rep., 2016.

[16] H. Jia, W. Xinjian, and S. Zechang, "Variable flux memory motors: A review," in *Transportation Electrification Asia-Pacific (ITEC Asia-Pacific), 2014 IEEE Conference and Expo*. IEEE, 2014, pp. 1–6.

[17] K. Sakai, K. Yuki, Y. Hashiba, N. Takahashi, and K. Yasui, "Principle of the variable-magnetic-force memory motor," in *Electrical Machines and Systems, 2009. ICEMS 2009. International Conference on*. IEEE, 2009, pp. 1–6.

[18] A. Athavale, K. Sasaki, B. S. Gagas, T. Kato, and R. D. Lorenz, "Variable flux permanent magnet synchronous machine (vf-pmsm) design to meet electric vehicle traction requirements with reduced losses," in *Energy Conversion Congress and Exposition (ECCE), 2016 IEEE*. IEEE, 2016, pp. 1–8.

[19] A. Athavale, K. Sasaki, T. Kato, and R. D. Lorenz, "Magnetization state estimation in variable-flux pmsms," in *Electric Machines and Drives Conference (IEMDC), 2017 IEEE International*. IEEE, 2017, pp. 1–8.

[20] A. Athavale, D. J. Erato, and R. D. Lorenz, "Enabling driving cycle loss reduction in variable flux pmsms via closed-loop magnetization state control," in *Energy Conversion Congress and Exposition (ECCE), 2017 IEEE*. IEEE, 2017, pp. 1932–1939.